PAPER

Check for updates

Pyrolysis behaviors dominated by the reaction–diffusion mechanism in the fluorine-free metal–organic decomposition process

Jiangtao Shi, [ID] [a] Yue Zhao,*[ab] Yue Wu,[a] Jingyuan Chu, [ID] [a] Xiao Tang, [ID] [c] Xiaohang Li,[c] Xin Yu,[b] Wei Wu,[a] Guangyu Jiang,[b] Hongli Suo[d] and Zhijian Jin[a]

Owing to the advantages of its environmentally friendly process and superior high growth rate, the fluorine-free metal–organic decomposition (FF-MOD) is a promising route for the growth of $REBa_2Cu_3O_{7-\delta}$ (REBCO, where RE is Y or other rare-earth elements) superconducting films. In this work, the pyrolysis behaviors dominated by the reaction–diffusion mechanism were investigated. Combining the atomic force microscopy and the nanoindentation analysis, we concluded that the strain generated by decomposition reactions plays a crucial role in defect formation. Due to the smooth release of the strain and enhancement of the mechanical properties, the defect-free film could be obtained under a fast process. However, an inhomogeneous microstructure along the film thickness was always found by cross-section observation, i.e., a dense layer at the top, while a porous layer was found at the bottom, being separated by a clear boundary. Accordingly, the one-dimensional reaction–diffusion model is proposed. In addition, the formation of such laminar structure is associated with different reaction mechanisms, depending on the diffusion of oxygen and evolved gases. Moreover, severe copper segregation was discerned in the dense layer, which would heavily affect the superconducting phase transformation. Remarkably, a high critical current density value exceeding 2 MA cm^{-2} (77 K, self-field) was achieved in the $GdBa_2Cu_3O_7$ films grown on the CeO_2 buffered technical substrates. This work provides deep insight into the pyrolysis behaviors of the FF-MOD route in view of the fabrication of REBCO superconducting films with high throughput.

1. Introduction

The second-generation of high-temperature superconducting tape (2G-HTS) is one of the most promising practical superconducting materials, represented by $REBa_2Cu_3O_{7-\delta}$ films (REBCO, where RE is Y or other rare-earth elements). 2G-HTS has been widely used in magnetic resonance imaging,[1] transmission cables,[2] wind power generators,[3] and superconducting fault current limiters.[4] Recently, there has been a more urgent demand for a larger capacity of production and for a higher performance of 2G-HTS in the compact fusion magnet applications. Deposition of the superconducting layer is a key process of the mass production of 2G-HTS tapes. Generally, there are two main routes for REBCO deposition, i.e., in situ and ex situ. In the former case, the film deposition proceeds together with the superconducting phase formation, such as pulse laser deposition and metal–organic chemical vapor deposition. In the latter case, the deposition and phase formation are performed separately, such as reactive evaporation and chemical solution deposition (CSD). Due to the completely different growth mechanism, the in situ deposition methods enable the precise modulation of the desirable microstructure, while the ex situ ones offer the possibility of a much higher growth rate (one or two orders higher than that in the in situ processes[5]), which have great potentials for the throughput increase.

Among all the film deposition techniques, the CSD method is considered to be a commonly used top-down approach for oxide film growth. It has exhibited great advantages, such as non-vacuum, precise composition control, low capital investment, and is especially scalability for large-area film deposition.[6–12] A variety of functional materials have achieved epitaxial growth on single crystals or single-crystal-like substrates.[13–16] Control of the microstructure at the atomic

[a] School of Electronic Information and Electrical Engineering, Shanghai JiaoTong University, 200240 Shanghai, People's Republic of China. E-mail: yuezhao@sjtu.edu.cn; Fax: +86-21-5441-5519; Tel: +86-21-50817399

[b] Shanghai Superconductor Technology Co., Ltd, 200240 Shanghai, People's Republic of China

[c] King Abdullah University of Science and Technology (KAUST), Advanced Semiconductor Laboratory, Thuwal, 23955-6900, Saudi Arabia

[d] College of Materials Science and Engineering, Beijing University of Technology, 100022 Beijing, People's Republic of China

level could be realized through simple coating and heat treatment processes.

As a branch of CSD, the metal–organic decomposition (MOD) method is widely used in the preparation of REBCO superconducting films. It can be generally divided into two main categories: trifluoroacetate-metal–organic decomposition (TFA-MOD) and the fluorine-free routes (FF-MOD). In the typical TFA-MOD method process, the high J_c values of exceeding 2 MA cm^{-2} (at 77 K, self-field) have been successfully demonstrated either on single crystal substrates or on technical substrates. However, the very long and complex pyrolysis history (*i.e.*, longer than 10 hours for one deposition, more than four steps), as well as the low growth rate at the calcination process (less than 2 nm s^{-1}) are two key issues.[17–19] In the industry, these drawbacks are somehow overcome. In addition, this technique has been successfully adopted by several vendors worldwide, such as the American Superconductor Corporation,[20] BASF Corporation,[21] and Shanghai Creative Superconductor.[22] Moreover, the strategy of how to introduce APCs to improve the in-filed performance is becoming a hot topic.[23–31] Compared with the traditional TFA-MOD method, one of the main features in the FF-MOD processes is the appearance of a large amount of liquid phase,[28,29,32,33] which would greatly accelerate the growth rate at the high-temperature crystallization process (up to 100 nm s^{-1}).[34] The Ba–Cu–O liquid phases also assist in the consumption of BaCO$_3$. J_c values exceeding 3 MA cm^{-2} (at 77 K, self-field) have been achieved on YBCO films by the FF-MOD method.[35,36] Additionally, FF-MOD has exhibited the feasibility of making superconducting joints, being a milestone for 2G-HTS applications under the persistent current mode.[37]

In FF-MOD processes, the growth mechanism during REBCO crystallization becomes clear. For the pyrolysis, only a few studies address the morphologic features under various conditions.[38] In order to ensure a smooth stress release, a conservative pyrolysis rate (slower than 1 °C min^{-1}) was selected in the previous studies, and the overall decomposition was rather long (>300 min).[35] It is known that the pyrolysis process involves complex physical and chemical reactions, such as volume shrinkage, strain release, gas diffusion, as well as elemental segregation. In the practical case, moreover, the rapid pyrolysis process is required for high throughput, leading to non-equilibrium chemical reactions. A serious overlap of reactions would make the process even more complicated. So far, there is no reaction–diffusion model available to understand these phenomena. Therefore, it is worthwhile to pay more attention to the pyrolysis processes in order to push this approach to the next step.

In our previous works, we proposed a simple FF-MOD precursor solution, and the high-quality YBCO films were successfully deposited on both LaAlO$_3$ single crystals and CeO$_2$ buffered technical substrates.[35,39] In this paper, the GdBa$_2$Cu$_3$O$_{7-\delta}$ (GdBCO) constitution is selected due to the higher critical temperature (T_c = 96 K) and a higher critical current density J_c under high magnetic fields.[40,41] We focused on the pyrolysis process, and especially investigated the effect of the strain release mechanism and the microstructure

inhomogeneity on the superconducting performance. The thermal decomposition behavior of the xerogel was analyzed by thermogravimetric analysis and differential scanning calorimetry (TG-DSC). The microstructure was characterized in the pyrolyzed films by means of atomic force microscope (AFM), scanning electron microscope (SEM), transmission electron microscope (TEM) and selected area electron diffraction (SAED). The composition distribution along the film thickness was analyzed by energy dispersive spectrometer (EDS) and secondary ion mass spectrometry (SIMS). Consequently, the reaction–diffusion model of pyrolysis was proposed. A correlation between the structure in the pyrolyzed films and the superconductivity in fully sintered films was also established.

2. Experimental

2.1. Specimen preparation

The detailed synthesis process of the propionate-based precursor solutions was previously reported elsewhere.[36] Briefly, the precursor solution was synthesized by simply mixing stoichiometric amounts (1:2:3) of Gd-, Ba-, and Cu-acetates into propionic acid in a flask. The flask of the reaction mixture was placed on a magnetic stir plate until all of the reagents completely dissolved. The total cation concentration was set to 1.5 M in the precursor solution. Textured metallic tapes with a configuration of CeO$_2$/LaMnO$_3$/IBAD–MgO/Y$_2$O$_3$/Al$_2$O$_3$/C276 (supplied by the Shanghai Superconductor Technology[42]) were used as the buffer layers. The precursor solution was coated on the substrate by using the dip-coating technique (the dip-coater was from Shanghai SAN-YAN Instrument Co., Ltd, SYDC-100) under a withdrawal speed of 1000 μm s^{-1}. In addition, the sintered superconducting films with a thickness of about 250 nm were obtained under this condition. After drying, the coated films were directly inserted into the furnace preheated at about 100 °C. In addition, the pyrolysis process was done by using different heating rates and temperatures in a humid oxygen flow. The typical conditions studied in this paper are listed in Table 1. The sintering and oxygenation were previously described in ref. 35. For thermal analysis, the GdBCO xerogel powder was prepared by drying the solution at 80 °C for 24 hours.

2.2. Characterizations

The TG and DSC measurements (simultaneous TG-DSC device, in a model STA 6000 from PerkinElmer) were carried out up to 500 °C with a heating rate of 5 °C min^{-1} in a flowing O$_2$ atmosphere. The mass of the xerogel powder was ~8 mg.

The surface morphology of the pyrolyzed film was investigated by AFM (Bruker Multimode 8) on a 20 × 20 μm^2 area. AFM images were analyzed by using a NanoScope Analysis apparatus from Bruker. A Nano Indenter system with a diamond Berkovich triangular pyramidal tip indenter (Agilent Nano Indenter G200) was used to carry out studies, following a continuous stiffness measurement technique. Poisson's ratio (ν) was set to 0.18. The contact stiffness S (N m^{-1}), elastic modulus (Young's modulus, E (GPa)) and hardness H (GPa)

Table 1 Summary of the mechanical properties in the pyrolyzed films and J_c values on the sintered films. For comparison, the reference data on the film deposited by the TFA-MOD route is also included

ID	Pyrolysis process (temperature, pyrolysis rate)	RMS (nm)	Strain (U, N m^{-1})	Hardness (H, GPa)	Elastic modulus (E, GPa)	J_c (MA cm^{-2})
A	350 °C, 10 °C min^{-1}	29.2	4×10^{-3}	2.4	118.3	0.4
B	450 °C, 10 °C min^{-1}	7.6	2×10^{-3}	3.3	133.5	2.2
C	450 °C, 1 °C min^{-1}	5.3	2.4×10^{-6}	5.9	157.8	1.2
D	450 °C, 5 °C min^{-1}	6.9	1.1×10^{-5}	—	—	1.8
E	400 °C, 10 °C min^{-1}	25.1	5.5×10^{-3}	—	—	1.5
Ref. 55	310 °C, 5 °C min^{-1}	—	—	0.5	40	3–4

were determined as a function of the nanoindentation contact depth from these measurements.[43] At least eight load-penetration curves were recorded for each specimen to ensure the measurement reliability.

The phase and crystallographic texture of the GdBCO films were characterized by using a four-circle XRD equipped with a two-dimensional detector (Bruker D8 Advance, Cu-Kα radiation, λ = 1.54 Å). The microstructure of the pyrolyzed and sintered GdBCO films were analyzed by SEM (Zeiss Auriga). In addition, the tilt correction of the cross-sectional image was done by using the buffer layer thickness.

J_c values at 77 K self-field were measured by PPMS (Quantum Design), and calculated based on the Bean model[44] using the opening of the hysteresis loops obtained under a magnetic field applied perpendicular to the plane of the films.

The TEM cross-sectional sample was prepared by conventional mechanical polishing and grinding, followed by ion milling. The TEM imaging, together with SAED and EDX, were performed using an aberration-corrected scanning transmission electron microscope (STEM, FEI Talos F200 X) with a double-tilt holder and a cold field emission source operated at 200 kV.

The elemental distribution along the film thickness was collected by a dynamic SIMS instrument from Hiden Analytical Company (Warrington, UK) operated at 10^{-9} Torr. A continuous Ar$^+$ beam of 3 keV energy was applied to sputter the surface, while the selected ions were sequentially collected by using a MAXIM spectrometer equipped with a quadrupole analyzer.

3. Results and discussion

3.1. Thermal decomposition of the xerogel powder

To establish the pyrolysis schedule, the decomposition behaviors of the GdBCO xerogel powder were studied. The TG-DSC analysis (Fig. 1) indicates that the weight loss takes place together with the endothermic reactions when elevating the temperature. In addition, the decomposition is almost complete at around 400 °C. The most intense endothermic peak occurs at 400 °C, while a broad bump is overlapped with several small peaks from 80 °C to 400 °C. According to the DTG curve, the total weight loss (about 49.7% up to 500 °C) is divided into four stages. In the first stage (below 180 °C), the weight loss is small (only 6.9%) and there are no significant endothermic peaks, followed by a plateau from 150 °C to 180 °C. This process is mainly related to the removal of the humid vapor and the residual solvents (i.e., propionic acid and acetic acid) that were
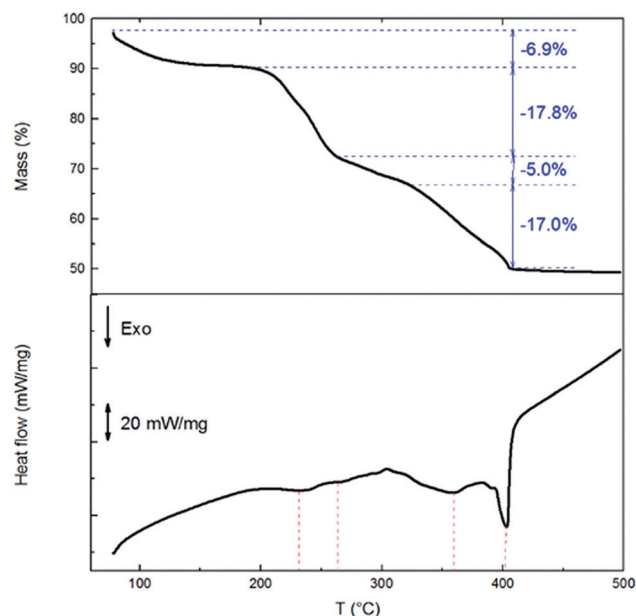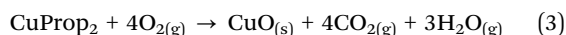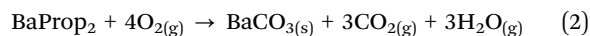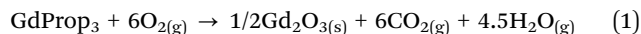

Fig. 1 Thermal decomposition of the GdBCO xerogel powder with a pyrolysis rate of 5 °C min^{-1} in a flowing O$_2$ gas: TG (upper panel) and corresponding DSC trace (lower panel).

not evaporated completely during the drying process. The second stage occurs at 180–260 °C together with a weak endothermic peak, and the weight loss reaches about 17.8%. According to the previous study on the propionate precursor,[36,45,46] it is deduced that the composition in the GdBCO xerogel powder mainly includes GdProp$_3$, BaProp$_2$ and CuProp$_2$. Decomposition of the individual chemicals have been extensively investigated,[46–49] which could provide informative clues to understand the decomposition of the GdBCO xerogel powder. For Cuprop$_2$, the most intense decomposition occurs below 250 °C, which is the lowest among all three propionates.[47] Therefore, we speculate that this stage is mainly associated with the CuProp$_2$ decomposition. The third and fourth stages occur at 260–310 °C and 310–390 °C, with corresponding weight losses of about 5% and 17%, respectively. Since all three propionates already start to decompose within this temperature window, it would be impossible to distinguish each reaction clearly. However, we notice an obvious endothermic peak at 400 °C, which is designated to the BaProp$_2$ decomposition. One should bear in mind that all three individual propionates decompose in the temperature range between 200 °C and 500 °C. Therefore, the reactions are seriously overlapped with each other,

which could be the explanation of the broad bump in the DSC trace.

An experimental total mass loss of 49.7% was found up to 500 °C. This agrees well with the theoretical value of 46.5% calculated from the following combustion reactions. As given below, the respective metal-salts transform into the simple oxides, $i.e.$, Gd_2O_3, $BaCO_3$, and CuO.

$$GdProp_3 + 6O_{2(g)} \rightarrow 1/2Gd_2O_{3(s)} + 6CO_{2(g)} + 4.5H_2O_{(g)} \quad (1)$$

$$BaProp_2 + 4O_{2(g)} \rightarrow BaCO_{3(s)} + 3CO_{2(g)} + 3H_2O_{(g)} \quad (2)$$

$$CuProp_2 + 4O_{2(g)} \rightarrow CuO_{(s)} + 4CO_{2(g)} + 3H_2O_{(g)} \quad (3)$$

It is worth noting that because of the significant small surface-to-volume ratio in powders compared to thin films, the xerogel powder decomposition is dramatically suppressed by the more difficult transport of the reactive gas from the surrounding atmosphere and out-diffusion of volatile products. It is reasonable to expect lower decomposition temperatures in the form of thin films. Anyway, the TG-DSC analysis could serve as a preliminary guideline. Thus, the maximum decomposition temperature was set to the range between 350 °C to 450 °C in the following study.

3.2. Strain and mechanical properties in the pyrolyzed film

During pyrolysis, a large mass loss leads to a dramatic physical change, $e.g.$, volume shrinkage, by more than 50% in most cases. Together with chemical reactions, as well as physical restriction of the substrate, it is inevitable to introduce inhomogeneous strain, either within the film plane or along the film thickness. In order to study the effect of the strain, AFM images were collected on the films prepared under different pyrolysis conditions, as shown in Fig. 2. The typical wrinkles and large height fluctuation were observed on the films prepared by conditions A, B and E (as shown in Table 1). Under the same pyrolysis rate of 10 °C min^{-1}, the RMS value decreases from 29.2 nm to 7.6 nm with an increase of the pyrolysis temperature. At the same pyrolysis temperature of 450 °C, the RMS values increase from 5.3 nm to 7.6 nm with an increase of the pyrolysis rate.

The main reason for the morphology difference in the film is the inhomogeneous strain release during pyrolysis. By carefully examining the microstructure (mainly the wrinkles, as well as the frequency and amplitude), the strain could be quantitatively estimated by eqn (4):

$$U = \frac{L - \lambda}{\lambda} \quad (4)$$

where L is the length of the fold in a period and λ is the wavelength. When the amplitude A is far less than λ, the above formula is transferred to eqn (5).[50,51]

$$U = \frac{L - \lambda}{\lambda} = \frac{A^2\pi^2}{\lambda^2} \quad (5)$$

By applying the fast Fourier transformation, λ and A can be obtained. In addition, the strain of the film under the compressive strain can be calculated. For example, in the film

prepared by condition A (denoted as A film), A is about 20 nm, and λ is about 1 μm. The results are shown in Table 1. The strain of the film gradually decreases with the increase of temperature (the strain (U) is 4×10^{-3} in the A film. Similarly, U is 5.5×10^{-3} and 2×10^{-3} in the E and B films), and increases with the increase of the pyrolysis rate (the strain (U) is 2.4×10^{-6} in the C film. U is 1.1×10^{-5} and 2×10^{-3} in the D and B films). It is seen that there is little change of the strain among the films prepared at various temperatures, while the pyrolysis rate plays a more important role (three orders of magnitude smaller at slow rate). However, one should bear in mind that the obvious wrinkles correspond to a large strain, but the effect on the superconducting phase transformation is still an open question. For the FF-MOD routes, a large amount of the liquid phase appears at the sintering process. A long diffusion distance of materials and the capillarity effect could make some defects self-healing, which will be discussed in Section 3.3.

To understand the defect formation, strain in the precursor film is also taken into consideration. It is known that in some cases, the strain would exceed 100 MPa, being associated with the volume shrinkage, mismatch of the substrate and gas release.[52] When exceeding the critical value, the strain is released as defects form, such as wrinkles and cracks. Neglecting the internal energy, the total energy associated with the crack is described in eqn (6):[53]

$$U_t = U_{se}^0 - [\sigma^2/(2E)]Zct^2 + G_cct \quad (6)$$

where U_{se}^0 is the initial strain energy within the crack-free film and Zct^2 is the volume of material around the crack, where strain energy is relieved. The energy needed to form the crack's surface is ctG_c, where G_c is the energy needed to form two crack surfaces in an area, and ct is the area of the crack. E is Young's modulus, ν is Poisson's ratio, Z is a dimensionless geometrical parameter, and σ is the biaxial tensile strain of the film. According to the reported concept,[54] a crack only extends if it reduces the free energy of the system, that is:

$$\partial U_t/\partial c = G_c t - Z[\sigma^2/(2E)]t^2 \leq 0 \quad (7)$$

It is deduced that, an increase of the elastic modulus E and decrease of the tensile strain σ would be favorable to obtain a defect-free film. Besides the precursor chemistry, the pyrolysis kinetics and mechanical properties of the film also play an important role in defect formation.

To further study the differences in the mechanical properties of the pyrolysis film, nano-indentation technology was used to obtain the constant stiffness, Young's modulus and the hardness. Fig. 3a shows the typical initial load-displacement curves recorded for three films under different pyrolysis processes (A, B and C films). Fig. 3b–d show that with the increase of the contact depth h, the stiffness (S), hardness (H) and elastic modulus (E) all gradually increase, and are indicative of the differences between the surface and the body in the films. This behavior is also observed in other CSD derived films,[55] probably due to the different kinetics related to the gas and
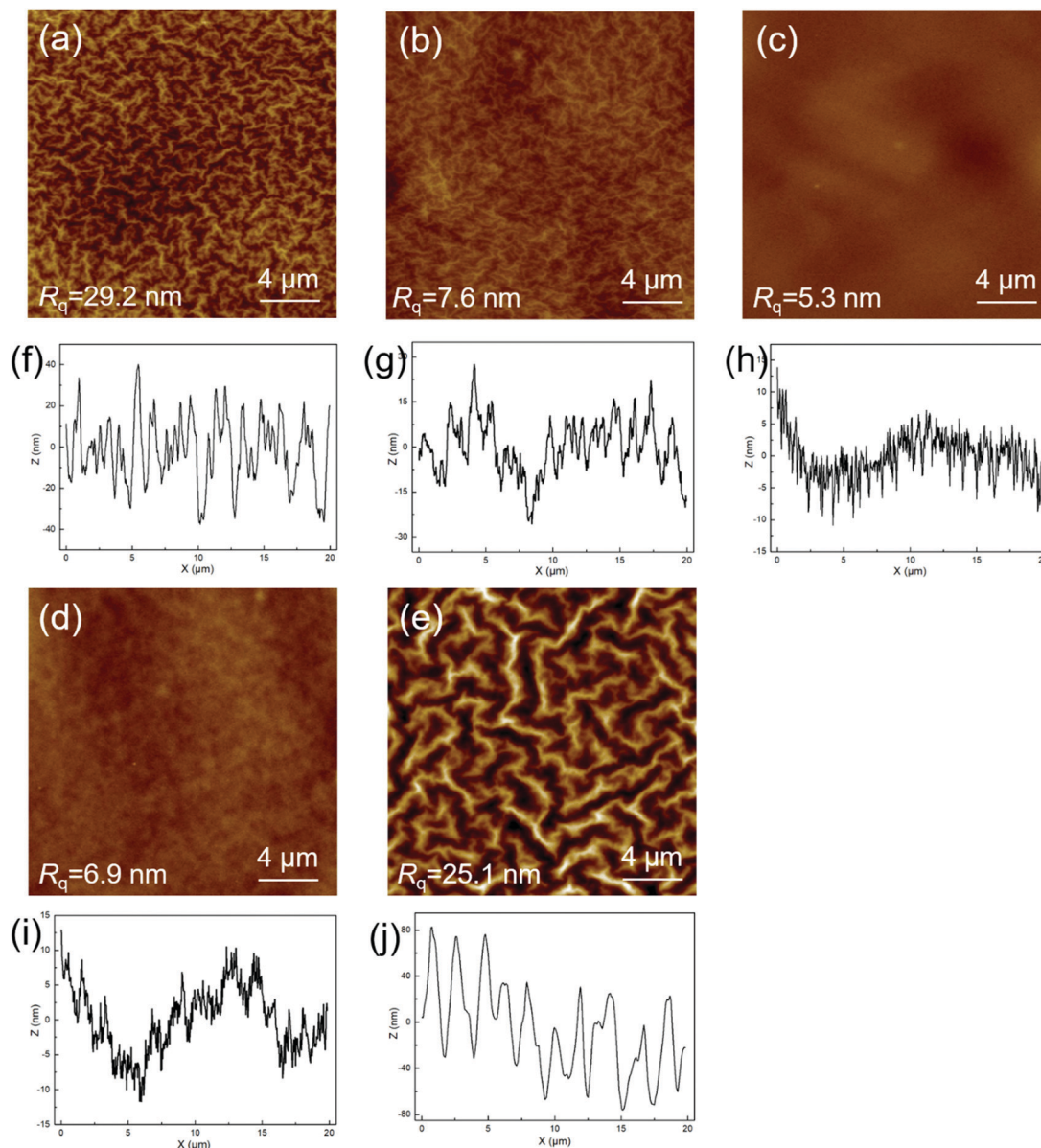
Fig. 2 AFM images and height profiles on the films prepared under different pyrolysis conditions: (a) and (f) by condition A. (b) and (g) by condition B, (c) and (h) by condition C, (d) and (i) by condition D, and (e) and (j) by condition E. Note that the RMS value is about 6 nm on the CeO_2 buffered technical substrates, serving as the baseline of the RMS value.

elemental diffusion. In the aspect of hardness (Fig. 3c), the pyrolysis temperature has little effect. However, the hardness significantly increases when the pyrolysis rate reduces from $10\ ^{\circ}C\ min^{-1}$ to $1\ ^{\circ}C\ min^{-1}$. Moreover, the hardness in the C film is about twice that in the B film (at a depth of 170 nm). In the aspect of the elastic modulus, it rises rapidly from the surface to the body with an increase of h, and reaches a plateau at a depth of 250 nm in the C film, while the elastic modulus does not appear to be saturated in either the A or B films. Actually, there is a minor difference in the three films at a depth of 350 nm. In summary, the pyrolysis rate has a more pronounced effect on the hardness and elastic modulus in the films.

Such mechanical properties are most likely related to the transfer of the soft gel to the hard oxide/amorphous state after decomposition. It is known that a gel film is within a porous network structure prior to pyrolysis, while the decomposition products are mixtures of oxides and amorphous, the mechanical properties of which are significantly enhanced. It is worth noting that during pyrolysis, the porous network structure provides a diffusion channel for the evolved gas, and the high viscosity also helps to densify, which also benefits the accommodation of the large strain. On the one hand, a fast pyrolysis rate of $10\ ^{\circ}C\ min^{-1}$ is more intensive and the internal strain is larger. Therefore, the release of an uneven distribution of compressive strain results in a wrinkle. On the other hand, at
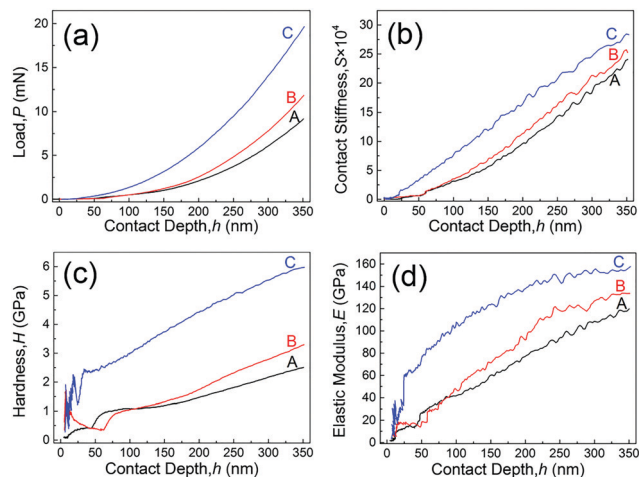
Fig. 3 Mechanical properties recorded on the films prepared under pyrolysis condition A, B and C. (a) The load-displacement trace, (b) the constant stiffness S, (c) the hardness H, and (d) the elastic modulus E as a function of the contact depth of the films are shown. Note that h is the penetration depth of the nanoindentation. Some fluctuations at a depth of 50 nm may be due to the uneven film surface.

Fig. 4 Crystallographic structure evolution of sintered films prepared under different pyrolysis conditions. Intensity of the GBCO (005) peak (a), and intensity of the GBCO (103) peak (b) with different dwell times.

Fig. 5 SEM images of the fully sintered GdBCO films: (a) and (b) on the A film, (c) on the B film, and (d) on the C film. The white, green, blue and red arrows point to the inclined plate-like structures, pores, irregular-shaped holes and copper-rich particles, respectively.

a high pyrolysis temperature, the strength of the film increases (*e.g.*, higher Young's modulus, higher hardness). This leads to the fact that the film could tolerate a rather large strain, consequently, no defect formation is found.

In addition, we found that the hardness values are 2–6 GPa in the pyrolyzed FF-MOD films, which is several times higher than those in the TFA-MOD films (as cited in Table 1). This might be caused by different pyrolysis processes and compositions. Due to the high strength of the pyrolyzed FF-MOD film, it is supposed that the defect formation could be avoided under a high pyrolysis rate, which is beneficial to increasing the throughput.

3.3. Effect of pyrolysis on the phase evolution

In this section, we further studied the phase and texture evolution of films under different pyrolysis conditions. The sintering process plays an important role in the nucleation and growth of REBCO. Interface reactions with the CeO$_2$ buffered technical substrates were also taken into consideration. GdBCO films were sintered with different dwell times under the identical temperature and pO$_2$ (at 780 °C with 50 ppm). Fig. 4a and b show the intensity of the GdBCO (005) and (103) reflections, by which the evolution of the *c*-oriented and polycrystalline texture component can be analyzed.

For the C film, the GdBCO phase and texture transition almost completes at 780 °C without any dwell time, which is evidenced by the strong GdBCO (005) and the negligible (103) peak. It takes at least 30 min to achieve the comparable intensity in the A and B films. Although it seems that all of the pyrolyzed film can form desirable structures under the optimal sintering conditions, the growth kinetics seemingly varies. The SEM observation reveals more microstructure details. As shown in Fig. 5, the fully sintered B and C films exhibit smooth and dense surfaces with few defects.
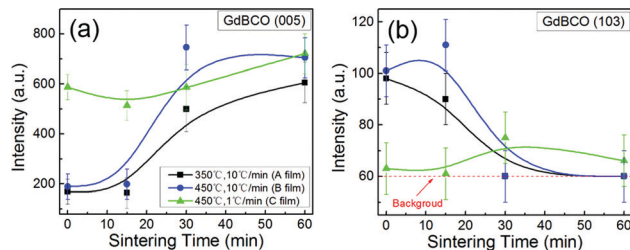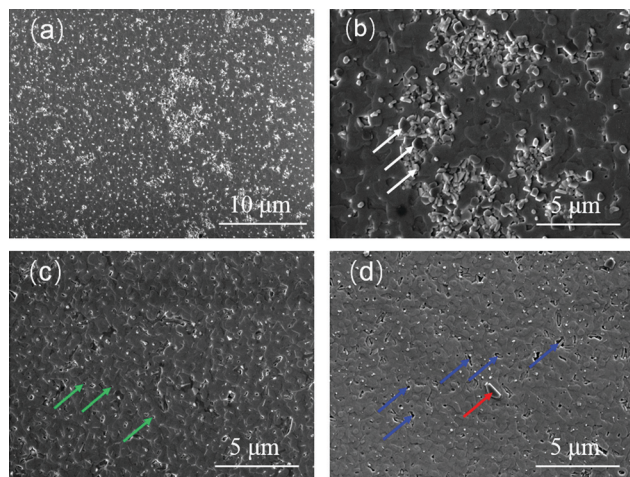
Such morphology is featured by the plated-like grains with meandering grain bounders, which are typical characteristics of the *c*-axis well-oriented REBCO prepared by FF-MOD routes. Moreover, the wrinkled feature observed in the pyrolyzed B film disappeared completely after sintering. In the sintered A film, however, besides plated-like grains, defective regions in the size of several micrometers were also observed, as indicated by white arrows in Fig. 5b. The zoomed-in image shows more of the defect features, *i.e.*, mainly inclined plated-like grains with smaller grain size, which corresponds to the randomly oriented GdBCO grains and intermediate phases. A longer dwell sintering time might be helpful to further push the reaction, while the interface reactions are also triggered, leading to a narrow processing window. In the sintered C film (Fig. 5d), there are some irregular-shaped holes, together with needle-like grains. Similar features are also found in the YBCO grown by FF-MOD routes.[35] Some small particles were also found on the surface of the sintered C film. These small particles are copper-rich, as confirmed by EDS, indicating that a slow pyrolysis rate leads to serious copper segregation.

In Table 1, we summarized the RMS values and mechanical properties in the pyrolyzed films, as well as their J_c values (at 77 K, self-field) after sintering. Reference data from a TFA-MOD

process is also included for comparison. A J_c value exceeding 2 MA cm^{-2} is achieved in the GBCO film prepared at 450 °C with a fast pyrolysis rate of 10 °C min^{-1}. Under the optimal conditions, for the films with J_c values exceeding 1 MA cm^{-2} (at 77 K, self-field), the T_c values are around 92.5 K.

3.4. Cross-sectional microstructure in the pyrolyzed films

According to the aforementioned results, it is known that the internal strain in the film increases with the increase of the pyrolysis rate. Generally, the smooth strain relief corresponds to a flat surface after pyrolysis, which would contribute to a high-quality REBCO film in most cases. Surprisingly, the J_c value in the film with high strain (2×10^{-3} in the B film) is almost double that with the small strain (2.4×10^{-6} in the C film), which is hardly explained by the strain relief mechanism.

To shed light on this behavior, we first investigated the cross-sectional microstructure in the films. From the SEM images (Fig. 6a–c), we found significant differences, *i.e.*, when the pyrolysis rate increases from 1 °C min^{-1} to 10 °C min^{-1}, the thickness of the pyrolyzed film is almost doubled (from 400 nm to 700 nm). Since the coating and the precursor solution are identical, the mass thicknesses of all three films are supposed to be comparable. Obviously, the significant difference in the geometric thickness is due to the porosity. Interestingly, it is noticed that there are two distinguished microstructural features along the thickness direction in all three films. A common feature of such laminar structure is a relatively dense layer at the top, and a porous one at the bottom (close to the substrate), which are separated by a clear boundary. By carefully checking the layer structure, it is seen that as the pyrolysis rate increases, the thickness proportion of the porous layer increases, while the porosity in the porous layer increases and the dimension of the pore increases (as summarized in Fig. 6d).

In order to further study the structural inhomogeneity and the composition distribution along the thickness direction,

we studied the cross-sectional microstructure on the B film by TEM. As shown in the HAADF image (Fig. 7a), the structural details in the dense layer and the porous layer are discerned, being in line with the cross-sectional SEM observation. The high-resolution image (Fig. 7b) reveals that the intermediate phases are mainly Gd_2O_3, $BaCO_3$ and CuO (confirmed by SAED). These phases are nanoparticles wrapped with an amorphous layer. Carefully comparing the diffraction patterns, we found that there are two broad rings in the SAED collected on the surface region, possibly corresponding to Gd_2CuO_4 and CuO reflections. A small amount of the Gd_2CuO_4 phase could be associated with the Gd_2O_3 and CuO reactions. In addition, it was noticed that the diffraction peaks close to the interface (Fig. 7e) are much sharper than those near the surface. This implies that the crystallinity is weaker in the surface layer, probably due to the reaction driving by enhanced diffusion machinimas in the surface layer.

We further analyzed the elemental distribution along the thickness direction by EDS, as shown in Fig. 8. Combining the ESD line-scan and microstructure characteristics analysis, it was found that serious copper segregation occurs in the surface layer (*i.e.*, in the dense layer). All of the other elements are rather homogenously distributed through the whole thickness. Surprisingly, the copper distribution is more uniform in the porous layer. A clear interface between the substrate and the film is an indication of no interface reactions.

In order to further confirm the element distribution, SIMS depth analysis was carried out on the B film. Compared with the EDS analysis in TEM, SIMS provides more statistical information due to a larger detective area (1 by 1 mm^2). Fig. 9a shows the distribution of C, Cu, Ba, Gd and Ce along the thickness. We noticed that the intensities of C, Gd and Ba exhibit similar trajectory, *i.e.*, a peak appears at a depth of about 230 nm. In particular, a strong dependence between C and Ba confirms the existence of $BaCO_3$ in the film. However,
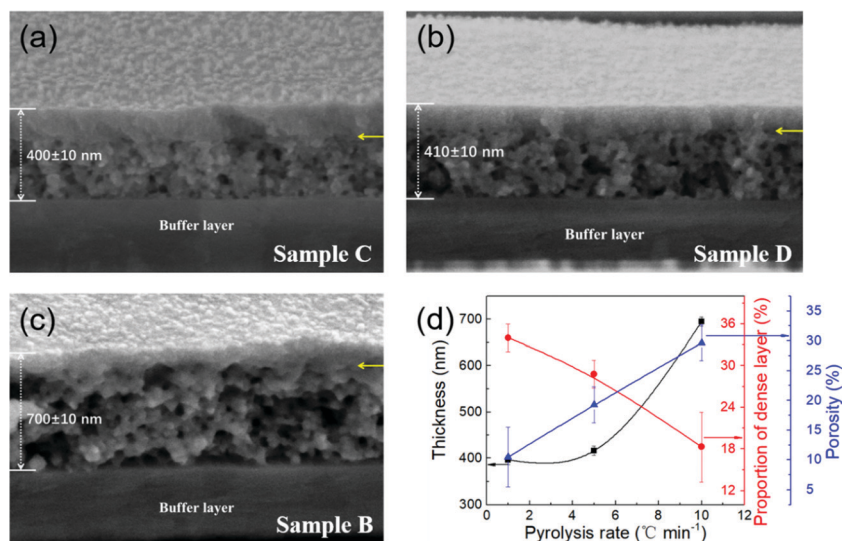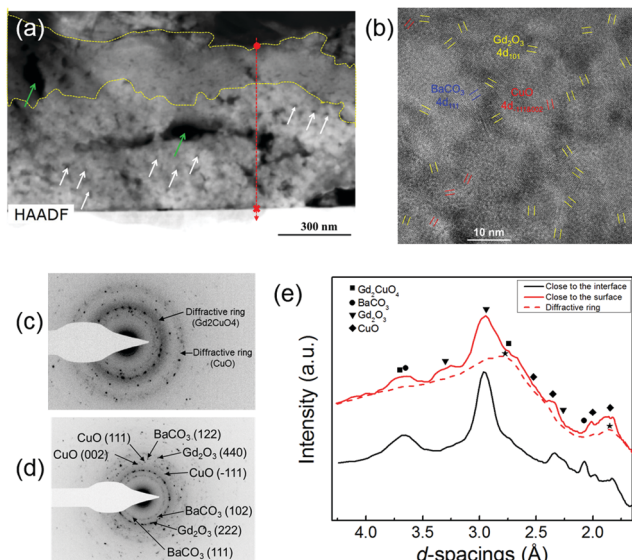

Fig. 6 Cross-sectional SEM images of the fully sintered GdBCO films. (a) On the C film, (b) on the D film, and (c) on the B film, where the yellow arrow shows the boundary. (d) Dependence of the film thickness, proportion of the dense layer, and the porosity with the pyrolysis rate.

Fig. 7 (a) Cross-section HAADF image of the pyrolyzed film. The white arrows point to the pin-holes in the film body, while the green arrow points to a defect caused by the TEM sample preparation. (b) High resolution TEM image, where the $BaCO_3$, Gd_2O_3, and CuO nanoparticles are marked by blue, yellow, and red, respectively. Selected area electron diffraction pattern in the surface layer (c) and in the bottom (d), respectively. (e) Integration intensity as a function of the d-spankings in the diffraction patterns, where the asterisks represent the diffraction rings shown in (c).
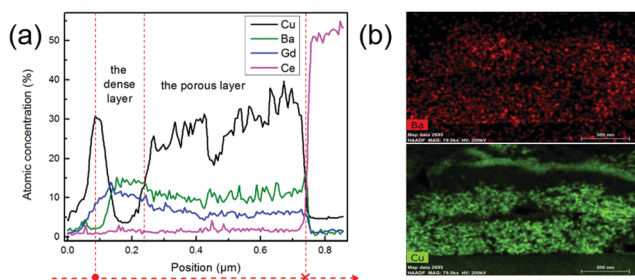
Fig. 8 EDS line scans along the thickness for Cu, Ba, Gd and Ce. (b) EDS mapping images for Ba and Cu.
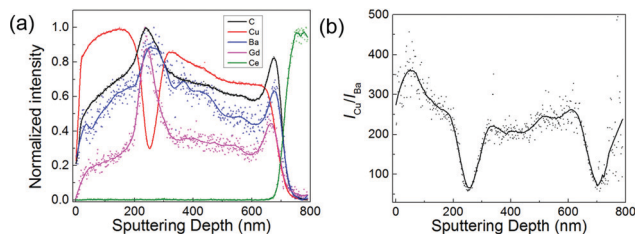
Fig. 9 SIMS spectral depth analysis on the pyrolyzed film: (a) elemental distribution of C, Cu, Ba, Gd, Ce, and (b) distribution of Cu/Ba ratio.

Cu exhibits a trace that is different from the others, *i.e.*, a valley appears at a depth of about 230 nm. To deeply understand this behavior, the ratio of Cu/Ba as a function of the depth is plotted in Fig. 9b, which avoids errors caused by the uneven surface.

Since the absolute count of ions depends on the yield of bombardment, a large Cu/Ba ratio (exceeding 300) does not indicate a serious off-stoichiometry. It can be further confirmed that the copper diffusion is rather complex along the thickness direction.

3.5. Reaction–diffusion model

To understand the laminar structure and elemental distribution, we established a one-dimensional reaction–diffusion model along the thickness. This model is strongly related to the chemical reactions dominated by diffusion of oxygen (pyrolysis atmosphere, also acting as a reactant gas) and the evolved gas. Fig. 10 shows the fundamental schematic of the reaction–diffusion model. In this model, the film is covered by a gas boundary layer, and the oxygen diffuses into the film through the boundary layer. The evolved gases diffuse out through the precursor boundary layer. The activity of O_2 (a_{O_2}) and the evolved gases (a_{gas}) in the diffusion boundary layer and the precursor are also given.

During pyrolysis, O_2 diffuses into the film as the process proceeds. Assuming that the O_2 diffusion source ($X_{O_2,g}$) is constant, the $a_{O_2,g}$ decreases gradually with the reaction consumption and with the increase of the diffusion distance, *i.e.*, a_{O_2} is higher in the surface than in the body. The evolved gases also easily diffuse out, so the exothermic reactions proceed with a large driving force in the surface layer. It is worth noting that relatively fast pyrolysis rates are applied in our study, which results in non-equilibrium conditions. This leads to the existence of a "neutral layer" (δ_n), where a_{O_2} gradually decreases to zero ($a_{O_2,n} = 0$). The δ_n position depends
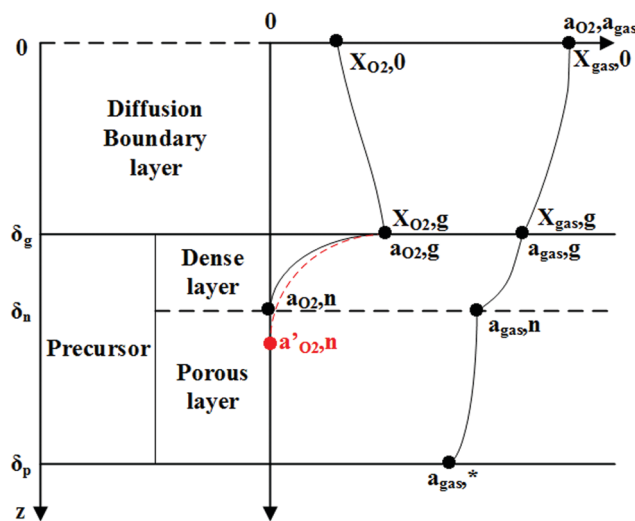
Fig. 10 Fundamental schematic of the one-dimensional reaction–diffusion model in the film. Here δ_g, δ_n and δ_p refer to the thickness of the diffusion boundary layer, dense layer and film, respectively. $X_{O_2,0}$ and $X_{O_2,g}$ refer to the humid O_2 flow away from the surface and on the film surface, respectively. $X_{gas,0}$ and $X_{gas,g}$ refer to the flow of the evolved gases away from the surface and on the film surface, respectively. a_{O_2} and a_{gas} refer to the activity of O_2 and the evolved gases released during pyrolysis. The red dash line in the precursor layer represents a change of a'_{O_2} under a slow pyrolysis rate.

on the pyrolysis rate. The neutral layer increasingly approaches the surface as the rate increases. Furthermore, the reaction condition switches to inert below δ_n, *i.e.*, the endothermic reactions are dominated. Rasia *et al.* studied the pyrolysis of propionate under different atmospheric conditions.[46,47] The results suggest that the decomposition of propionate is delayed under an inert atmosphere (*e.g.*, N_2), and the reaction takes place more smoothly than that in an oxygen atmosphere. Under an inert atmosphere, the propionates mainly occur along the radical decomposition reaction path, resulting in the release of symmetrical ketones. This results in completely different reactions occurring above and below δ_n. It is also the main reason why a clear boundary always appears in all of our cases.

Due to the different reaction mechanism along the thickness, the evolved gases and diffusion behaviors vary. Close to the substrate, there is no sufficient O_2, and the radical decomposition reactions dominate. The evolved gases therefore are easily trapped in the matrix. One should also keep in mind that the precursor film still has high elasticity due to the polymer-like 3D network structure. A large amount of trapped gases does not make the film collapse (no defects discerned), but only increases the film thickness. In the surface layer, the short gas diffusion path allows for easier densification.

With respect to the elemental distribution, it is reasonable that copper segregation is associated with its sublimation, which commonly occurs in the other processes.[56,57] Humid O_2 gas, of course, is favorable to suppress the segregation. In the surface layer (dense layer), the short diffusion path leads to serious copper segregation, which is not evident in the porous layer thanks to the long diffusion distance and the delayed reactions. It is known that the formation of REBCO is a process where RE dissolves into the Ba–Cu–O transient liquid in the FF-MOD route. The appearance of such liquid with complex compositions depends on the deposition temperature and the Ba/Cu stoichiometry. For example, in the O_2 atmosphere, the eutectic temperature of Ba–Cu is 920 °C at Ba/Cu = 3 : 7, while it can be as high as 1010 °C at Ba/Cu = 2 : 3.[58,59] Obviously, the copper segregation causes the liquid phase to appear at low temperature in the surface layer, which leads to poor epitaxy and the inhomogeneity of phase formation. As a result, this seriously affects the GdBCO film quality.

When going back to the question raised at the end of Section 3.4, the answer is given as follows. In our case, the thickness is always about 250 nm in sintered films regardless of the pyrolysis processes, and there is no significant difference in crystallinity. This indicates that the porous structure does not obviously affect the formation of the superconducting phase. In the FF-MOD process, the precursor film would form a large amount of enhanced Ba–Cu–O transient liquid during sintering, which is helpful for the structural reorganization, *i.e.*, densification. Improvement of the superconductivity in the film prepared under a higher pyrolysis rate is most likely attributed to the uniform distribution of the composition along the thickness direction.

4. Conclusions

In this work, we investigated the pyrolysis behavior in the FF-MOD method. First, the effects of pyrolysis processes on the morphology and mechanical properties in the films were studied. In view of increasing the throughput, a rapid pyrolysis procedure that is less than 40 min is demonstrated based on the smooth strain release mechanism and enhancement of the mechanical properties. As a result, the defect-free film is obtained under a high pyrolysis rate of 10 °C min^{-1}. Secondly, the cross-sectional morphology in the pyrolyzed film was observed and characterized comprehensively. The laminar structure with a dense layer in the surface and a porous layer in the bottom are always discerned. Moreover, elemental analysis along the thickness shows that copper segregation in the dense layer is more serious in the porous layer. Such features probably have a strong influence on the Ba–Cu–O liquid phase formation. Therefore, the quality of the superconducting film varies. Accordingly, a reaction–diffusion model is proposed. It is found that the diffusion behaviors of oxygen and the evolved gases play an important role. In addition, a neutral layer between the dense and porous layer exists. The decomposition reactions differ above and below this neutral layer. Remarkably, a high J_c value exceeding 2 MA cm^{-2} (77 K, self-field) was achieved in the GdBCO film grown on the technical substrates.

Conflicts of interest

There are no conflicts to declare.

Acknowledgements

References

1 W. D. Markiewicz, D. C. Larbalestier, H. W. Weijers, A. J. Voran, K. W. Pickard, W. R. Sheppard, J. Jaroszynski, X. Aixia, R. P. Walsh, L. Jun, A. V. Gavrilin and P. D. Noyes, Design of a Superconducting 32 T Magnet With REBCO High Field Coils, *IEEE Trans. Appl. Supercond.*, 2012, **22**(3), 4300704, DOI: 10.1109/TASC.2011.2174952.

2 X. Wang, D. R. Dietderich, J. DiMarco, W. B. Ghiorso, S. A. Gourlay, H. C. Higley, A. Lin, S. O. Prestemon, D. v. d. Laan and J. D. Weiss, A 1.2 T canted cosθ dipole magnet using high-temperature superconducting CORC®

wires, *Supercond. Sci. Technol.*, 2019, **32**(7), 075002, DOI: 10.1088/1361-6668/ab0eba.

3 H.-J. Sung, M. Park, B.-S. Go and I.-K. Yu, A study on the required performance of a 2G HTS wire for HTS wind power generators, *Supercond. Sci. Technol.*, 2016, **29**(5), 054001, DOI: 10.1088/0953-2048/29/5/054001.

4 M. Majka, J. Kozak and S. Kozak, HTS Tapes Selection for Superconducting Current Limiters, *IEEE Trans. Appl. Supercond.*, 2017, **27**(4), 5601405, DOI: 10.1109/TASC.2017.2669191.

5 S.-I. Yoo, Processing-microstructure-property relationship in $GdBa_2Cu_3O_{7-d}$ coated conductors via the RCE-DR Process, in *9th Workshop on Mechanical and Electromagnetic Properties of Composite Superconductors*, Andong, Korea, 2018.

6 F. Lange, Chemical solution routes to single-crystal thin films, *Science*, 1996, **273**(5277), 903–909, DOI: 10.1002/chin.199649283.

7 X. Obradors, T. Puig, A. Pomar, F. Sandiumenge, N. Mestres, M. Coll, A. Cavallaro, N. Romà, J. Gázquez, J. C. González, O. Castaño, J. Gutierrez, A. Palau, K. Zalamova, S. Morlens, A. Hassini, M. Gibert, S. Ricart, J. M. Moretó, S. Piñol, D. Isfort and J. Bock, Progress towards all-chemical superconducting YBa2Cu3O7-coated conductors, *Supercond. Sci. Technol.*, 2006, **19**(3), S13–S26, DOI: 10.1088/0953-2048/19/3/003.

8 R. W. Schwartz, T. Schneller and R. Waser, Chemical solution deposition of electronic oxide films, *C. R. Chim*, 2004, **7**(5), 433–461, DOI: 10.1016/j.crci.2004.01.007.

9 S. Starschich, D. Griesche, T. Schneller, R. Waser and U. Böttger, Chemical solution deposition of ferroelectric yttrium-doped hafnium oxide films on platinum electrodes, *Appl. Phys. Lett.*, 2014, **104**(20), 202903, DOI: 10.1063/1.4879283.

10 A. Zarkov, A. Stanulis, L. Mikoliunaite, A. Katelnikovas, V. Jasulaitiene, R. Ramanauskas, S. Tautkus and A. Kareiva, Chemical solution deposition of pure and Gd-doped ceria thin films: Structural, morphological and optical properties, *Ceram. Int.*, 2017, **43**(5), 4280–4287, DOI: 10.1016/j.ceramint.2016.12.070.

11 D. Cabrera-German, J. A. García-Valenzuela, M. Cota-Leal, M. Martínez-Gil, R. Aceves and M. Sotelo-Lerma, Detailed characterization of good-quality SnS thin films obtained by chemical solution deposition at different reaction temperatures, *Mater. Sci. Semicond. Process.*, 2019, **89**, 131–142, DOI: 10.1016/j.mssp.2018.09.009.

12 W. T. Wang, G. Li, M. H. Pu, R. P. Sun, H. M. Zhou, Y. Zhang, H. Zhang, Y. Yang, C. H. Cheng and Y. Zhao, Chemical solution deposition of YBCO thin film by different polymer additives, *Phys. C*, 2008, **468**, 1563–1566, DOI: 10.1016/j.physc.2008.05.067.

13 X. Huang, Z. Zeng, S. Bao, M. Wang, X. Qi, Z. Fan and H. Zhang, Solution-phase epitaxial growth of noble metal nanostructures on dispersible single-layer molybdenum disulfide nanosheets, *Nat. Commun.*, 2013, **4**, 1444, DOI: 10.1038/ncomms2472.

14 C. H. Lee, T. Schiros, E. J. Santos, B. Kim, K. G. Yager, S. J. Kang, S. Lee, J. Yu, K. Watanabe, T. Taniguchi, J. Hone, E. Kaxiras, C. Nuckolls and P. Kim, Epitaxial growth of molecular crystals on van der Waals substrates for high-performance organic electronics, *Adv. Mater.*, 2014, **26**(18), 2812–2817, DOI: 10.1002/adma.201304973.

15 M. V. Kelso, N. K. Mahenderkar, Q. Chen, J. Z. Tubbesing and J. A. Switzer, Spin coating epitaxial films, *Science*, 2019, **364**(6436), 166–169, DOI: 10.1126/science.aaw6184.

16 O. L. Muskens, S. L. Diedenhofen, M. H. M. van Weert, M. T. Borgström, E. P. A. M. Bakkers and J. G. Rivas, Epitaxial Growth of Aligned Semiconductor Nanowire Metamaterials for Photonic Applications, *Adv. Funct. Mater.*, 2008, **18**(7), 1039–1046, DOI: 10.1002/adfm.200701337.

17 H. Chen, F. Feng, T. M. Qu and Z. Han, The study of a rotating method for fabricating Y1Ba2Cu3O7−x films by TFA-MOD, *Phys. C*, 2008, **468**(15–20), 1869–1872, DOI: 10.1016/j.physc.2008.05.205.

18 H. Chen, K. Zalamova, A. Pomar, X. Granados, T. Puig and X. Obradors, Growth rate control and solid–gas modeling of TFA-YBa2Cu3O7 thin film processing, *Supercond. Sci. Technol.*, 2010, **23**(3), 034005, DOI: 10.1088/0953-2048/23/3/034005.

19 M. Erbe, J. Hänisch, T. Freudenberg, A. Kirchner, I. Mönch, S. Kaskel, L. Schultz and B. Holzapfel, Improved REBa2Cu3O7−x (RE = Y, Gd) structure and superconducting properties by addition of acetylacetone in TFA-MOD precursor solutions, *J. Mater. Chem. A*, 2014, **2**(14), 4932–4944, DOI: 10.1039/c3ta15243j.

20 M. W. Rupich, X. Li, C. Thieme, S. Sathyamurthy, S. Fleshler, D. Tucker, E. Thompson, J. Schreiber, J. Lynch and D. Buczek, Advances in second generation high temperature superconducting wire manufacturing and R&D at American Superconductor Corporation, *Supercond. Sci. Technol.*, 2009, **23**(1), 014015, DOI: 10.1088/0953-2048/23/1/014015.

21 M. Witte, G. Gottstein, N. de Boer, S. Gilges, J. Klöwer, M. Bäcker, O. Brunkahl, B. Wojtyniak, W. Mader and M. Svete, The project SupraMetall: towards commercial fabrication of high-temperature superconducting tapes, *Adv. Eng. Mater.*, 2014, **16**(5), 539–549, DOI: 10.1002/adem.201300415.

22 Y. M. Lu, C. B. Cai, Z. Y. Liu, Y. Q. Guo, H. B. Jiang, Y. J. Zhang, M. J. Li, F. Fan, C. Y. Bai, Q. Lu, W. Z. Dou and W. Yang, Advance in Long-Length REBCO Coated Conductors Prepared by Reel-to-Reel Metalorganic Solution and Ion-Beam-Assisted Deposition, *IEEE Trans. Appl. Supercond.*, 2019, **29**(5), 6602805, DOI: 10.1109/TASC.2019.2910021.

23 M. Erbe, J. Hänisch, R. Hühne, T. Freudenberg, A. Kirchner, L. Molina-Luna, C. Damm, G. Van Tendeloo, S. Kaskel, L. Schultz and B. Holzapfel, BaHfO3 artificial pinning centres in TFA-MOD-derived YBCO and GdBCO thin films, *Supercond. Sci. Technol.*, 2015, **28**(11), 114002, DOI: 10.1088/0953-2048/28/11/114002.

24 K. Kimura, R. Hironaga, Y. Takahashi, T. Nakanishi, T. Koizumi, T. Hasegawa, K. Higashikawa, M. Inoue, T. Kiss, T. Kato, T. Nakamura, M. Yoshizumi, T. Izumi

and Y. Shiohara, Development of REBCO Coated Conductors by TFA-MOD Method With High Characteristic in Magnetic Field, *IEEE Trans. Appl. Supercond.*, 2013, **23**(3), 6601704, DOI: 10.1109/TASC.2013.2238975.

25 K. Nakaoka, R. Yoshida, K. Kimura, T. Kato, Y. Usui, T. Izumi and Y. Shiohara, Another approach for controlling size and distribution of nanoparticles in coated conductors fabricated by the TFA-MOD method, *Supercond. Sci. Technol.*, 2017, **30**(5), 055008, DOI: 10.1088/1361-6668/aa66e1.

26 T. Izumi and K. Nakaoka, Control of artificial pinning centers in REBCO coated conductors derived from the trifluoroacetate metal-organic deposition process, *Supercond. Sci. Technol.*, 2018, **31**(3), 034008, DOI: 10.1088/1361-6668/aa9dd2.

27 T. Nishiyama, K. Kaneko, K. Yamada, R. Teranishi, T. Kato, T. Hirayama, T. Izumi and Y. Shiohara, Microstructural characterization of TFA-MOD processed Y((1)-x)Gd(x)Ba-(2)Cu(3)O((7)-y) with BaZrO(3), *Micron*, 2013, **52–53**, 1–7, DOI: 10.1016/j.micron.2013.06.010.

28 T. Motoki, S. Ikeda, S.-i. Nakamura, G. Honda, T. Nagaishi, T. Doi and J.-i. Shimoyama, Greatly enhanced flux pinning properties of fluorine-free metal–organic decomposition YBCO films by co-addition of halogens (Cl, Br) and metals (Zr, Sn, Hf), *Supercond. Sci. Technol.*, 2018, **31**(4), 044004, DOI: 10.1088/1361-6668/aaae95.

29 H. Yamasaki, K. Ohki, I. Yamaguchi, M. Sohma, W. Kondo, H. Matsui, T. Manabe and T. Kumagai, Strong flux pinning due to dislocations associated with stacking faults in Y $Ba_2Cu_3O_{7-\delta}$ thin films prepared by fluorine-free metal organic deposition, *Supercond. Sci. Technol.*, 2010, **23**(10), 105004, DOI: 10.1088/0953-2048/23/10/105004.

30 X. Tang, Y. Zhao, W. Wu and J. C. Grivel, Effect of BaZrO3/Ag hybrid doping to the microstructure and performance of fluorine-free MOD method derived YBa2Cu3O7-x superconducting thin films, *J. Mater. Sci.: Mater. Electron.*, 2014, **26**(3), 1806–1811, DOI: 10.1007/s10854-014-2614-7.

31 P. Cayado, M. Erbe, S. Kauffmann-Weiss, C. Bühler, A. Jung, J. Hänisch and B. Holzapfel, Large critical current densities and pinning forces in CSD-grown superconducting GdBa2Cu3O7−x-BaHfO3 nanocomposite films, *Supercond. Sci. Technol.*, 2017, **30**(9), 094007, DOI: 10.1088/1361-6668/aa7e47.

32 J. Chu, Y. Zhao, M. Z. Khan, X. Tang, W. Wu, J. Shi, Y. Wu, H. Huhtinen, H. Suo and Z. Jin, Insight into the Interfacial Nucleation and Competitive Growth of YBa2Cu3O7−δ Films as High-Performance Coated Conductors by a Fluorine-Free Metal–Organic Decomposition Route, *Cryst. Growth Des.*, 2019, **19**(11), 6752–6762, DOI: 10.1021/acs.cgd.9b01120.

33 T. Araki and I. Hirabayashi, Review of a chemical approach to YBa2Cu3O7−x-coated superconductors—metalorganic deposition using trifluoroacetates, *Supercond. Sci. Technol.*, 2003, **16**(11), R71, DOI: 10.1088/0953-2048/16/11/R01.

34 L. Soler, J. Jareno, J. Banchewski, S. Rasi, N. Chamorro, R. Guzman, R. Yanez, C. Mocuta, S. Ricart, J. Farjas, P. Roura-Grabulosa, X. Obradors and T. Puig, Ultrafast transient liquid assisted growth of high current density superconducting films, *Nat. Commun.*, 2020, **11**(1), 344, DOI: 10.1038/s41467-019-13791-1.

35 J. Chu, Y. Zhao, Y. Ji, W. Wu, J. Shi, Z. Hong, L. Ma, H. Suo and Z. Jin, Interface reaction-governed heteroepitaxial growth of YBa2Cu3O7-δ film on CeO2-buffered technical substrate, *J. Am. Ceram. Soc.*, 2019, **102**(10), 5705–5715, DOI: 10.1111/jace.16452.

36 Y. Zhao, P. Torres, X. Tang, P. Norby and J. C. Grivel, Growth of Highly Epitaxial YBa2Cu3O(7-delta) Films from a Simple Propionate-Based Solution, *Inorg. Chem.*, 2015, **54**(21), 10232–10238, DOI: 10.1021/acs.inorgchem.5b01486.

37 K. Ohki, T. Nagaishi, T. Kato, D. Yokoe, T. Hirayama, Y. Ikuhara, T. Ueno, K. Yamagishi, T. Takao, R. Piao, H. Maeda and Y. Yanagisawa, Fabrication, microstructure and persistent current measurement of an intermediate grown superconducting (iGS) joint between REBCO-coated conductors, *Supercond. Sci. Technol.*, 2017, **30**(11), 115017, DOI: 10.1088/1361-6668/aa8e65.

38 L. H. Jin, Y. F. Lu, J. Q. Feng, S. N. Zhang, Z. M. Yu, Y. Wang and C. S. Li, Development of modified TFA-MOD approach for GdBa2Cu3Oy film growth, *Mater. Lett.*, 2013, **94**, 23–26, DOI: 10.1016/j.matlet.2012.12.022.

39 Y. Zhao, J. Chu, T. Qureishy, W. Wu, Z. Zhang, P. Mikheenko, T. H. Johansen and J.-C. Grivel, Structural and superconducting characteristics of YBa 2 Cu 3 O 7 films grown by fluorine-free metal-organic deposition route, *Acta Mater.*, 2018, **144**, 844–852, DOI: 10.1016/j.actamat.2017.11.050.

40 Y. Xu, M. Izumi, K. Tsuzuki, Y. Zhang, C. Xu, M. Murakami, N. Sakai and I. Hirabayashi, Flux pinning properties in a GdBa2Cu3O7−δ bulk superconductor with the addition of magnetic alloy particles, *Supercond. Sci. Technol.*, 2009, **22**(9), 095009, DOI: 10.1088/0953-2048/22/9/095009.

41 S. Rosenzweig, J. Hänisch, K. Iida, A. Kauffmann, C. Mickel, T. Thersleff, J. Freudenberger, R. Hühne, B. Holzapfel and L. Schultz, Irreversibility field up to 42 T of GdBa2Cu3O7-δthin films grown by PLD and its dependence on deposition parameters, *Supercond. Sci. Technol.*, 2010, **23**(10), 105017, DOI: 10.1088/0953-2048/23/10/105017.

42 Y. Zhao, J. M. Zhu, G. Y. Jiang, C. S. Chen, W. Wu, Z. W. Zhang, S. K. Chen, Y. M. Hong, Z. Y. Hong, Z. J. Jin and Y. Yamada, Progress in fabrication of second generation high temperature superconducting tape at Shanghai Superconductor Technology, *Supercond. Sci. Technol.*, 2019, **32**(4), 044004, DOI: 10.1088/1361-6668/aafea5.

43 X. Li and B. Bhushan, A review of nanoindentation continuous stiffness measurement technique and its applications, *Mater. Charact.*, 2002, **48**(1), 11–36, DOI: 10.1016/S1044-5803(02)00192-4.

44 H. P. Wiesinger, F. M. Sauerzopf and H. W. Weber, On the calculation of Jc from magnetization measurements on superconductors, *Phys. C*, 1992, **203**(1–2), 121–128, DOI: 10.1016/0921-4534(92)90517-G.

45 M. Nasui, T. Petrisor, R. B. Mos, M. S. Gabor, A. Mesaros, F. Goga, L. Ciontea and T. Petrisor, Fluorine-free propionate route for the chemical solution deposition of YBa2Cu3O7−x superconducting films, *Ceram. Int.*, 2015, **41**(3), 4416–4421, DOI: 10.1016/j.ceramint.2014.11.132.

46 S. Rasi, S. Ricart, X. Obradors, T. Puig, P. Roura-Grabulosa and J. Farjas, Radical and oxidative pathways in the pyrolysis of a barium propionate-acetate salt, *J. Anal. Appl. Pyrolysis*, 2019, **141**, 104640, DOI: 10.1016/j.jaap.2019.104640.

47 S. Rasi, F. Silveri, S. Ricart, X. Obradors, T. Puig, P. Roura-Grabulosa and J. Farjas, Thermal decomposition of CuProp2: In-situ analysis of film and powder pyrolysis, *J. Anal. Appl. Pyrolysis*, 2019, **140**, 312–320, DOI: 10.1016/j.jaap.2019.04.008.

48 J. C. Grivel, Thermal decomposition of RE(C2H5CO2)3·H2O (RE = Dy, Tb, Gd, Eu and Sm), *J. Therm. Anal. Calorim.*, 2013, **115**(2), 1253–1264, DOI: 10.1007/s10973-013-3467-7.

49 S. Rasi, S. Ricart, X. Obradors, T. Puig, P. Roura-Grabulosa and J. Farjas, Effect of triethanolamine on the pyrolysis of metal-propionate-based solutions, *J. Anal. Appl. Pyrolysis*, 2019, **143**, 104685, DOI: 10.1016/j.jaap.2019.104685.

50 P. J. Yoo, K. Y. Suh, S. Y. Park and H. H. Lee, Physical Self-Assembly of Microstructures by Anisotropic Buckling, *Adv. Mater.*, 2002, **14**(19), 1383–1387, DOI: 10.1002/1521-4095(20021002)14:19<1383::AID-ADMA1383>3.0.CO;2-D.

51 J. Groenewold, Wrinkling of plates coupled with soft elastic media, *Physica A*, 2001, **298**(1–2), 32–45, DOI: 10.1016/S0378-4371(01)00209-6.

52 T. J. Garino and M. Harrington, Residual Stress in Pzt Thin Films and its Effect on Ferroelectric Properties, *MRS Proc.*, 1991, **243**, 341–347, DOI: 10.1557/proc-243-341.

53 F. F. Lange, Chemical Solution Routes to Single-Crystal Thin Films, *Science*, 1996, **27**(49), 1, DOI: 10.1002/chin.199649283.

54 A. A. Griffith, The phenomena of rupture and flow in solids, *Philos. Trans. R. Soc., A*, 1921, **221**, 163–198, DOI: 10.1098/rsta.1921.0006.

55 K. Zalamova, N. Romà, A. Pomar, S. Morlens, T. Puig, J. Gázquez, A. E. Carrillo, F. Sandiumenge, S. Ricart, N. Mestres and X. Obradors, Smooth Stress Relief of Trifluoroacetate Metal-Organic Solutions for YBa2Cu3O7 Film Growth, *Chem. Mater.*, 2006, **18**(25), 5897–5906, DOI: 10.1021/cm061556+.

56 T. Izumi and K. Nakaoka, Control of artificial pinning centers in REBCO coated conductors derived from the trifluoroacetate metal-organic deposition process, *Supercond. Sci. Technol.*, 2018, **31**(3), 034008, DOI: 10.1088/1361-6668/aa9dd2.

57 K. Nakaoka, R. Yoshida, K. Kimura, T. Kato, Y. Usui, T. Izumi and Y. Shiohara, Another approach for controlling size and distribution of nanoparticles in coated conductors fabricated by the TFA-MOD method, *Supercond. Sci. Technol.*, 2017, **30**(5), 055008, DOI: 10.1088/1361-6668/aa66e1.

58 M. Nevřiva, E. Pollert, L. Matějková and A. Tříska, On the determination of the CuO-BaCuO2 and CuO-YCuO2.5 binary phase diagrams, *J. Cryst. Growth*, 1988, **91**(3), 434–438, DOI: 10.1016/0022-0248(88)90265-5.

59 P.-Y. Chu and R. C. Buchanan, Reactive liquid phase sintering of solution-derived YBa2Cu3O7−x superconducting thin films: Part I. Ambient and precursor effects on BaO–CuO liquid phase formation, *J. Mater. Res.*, 1993, **8**(9), 2134–2142, DOI: 10.1557/JMR.1993.2134.